FLOW FILED OF NON-NEWTONIAN FLUIDS IN IMPINGING JETS CONFINED BY SLOPPING PLANE WALLS

Adélio S. Cavadas[1], Fernando T. Pinho[1,2], João B.L.M. Campos[3]

1: Centro de Estudos de Fenómenos de Transporte, Faculdade de Engenharia da Universidade do Porto, Rua Dr. Roberto Frias s/n, 4200-465 Porto, Portugal, adelioc@fe.up.pt
2: Universidade do Minho, Largo do Paço, 4704-553 Braga, Portugal, fpinho@fe.up.pt
3: Centro de Estudos de Fenómenos de Transporte, Departamento de Engenharia Química, Faculdade de Engenharia da Universidade do Porto, Rua Dr. Roberto Frias s/n, 4200-465 Porto, Portugal, jmc@fe.up.pt

Abstract An experimental investigation was carried out to characterize the flow field in a liquid impinging jet confined by slopping plane walls and emanating from a rectangular duct for various non-Newtonian fluids. These jets are frequently found in processes within the food and pharmaceutical industries, and they are formed when a high velocity fluid impinges a solid surface leading to intense levels of heat and mass transfer. The experimental work is complemented by results from a numerical investigation for purely viscous fluids. This work continues previous research, Cavadas et al (2006), on the same flow geometry for Newtonian fluids in laminar and turbulent flow regimes. Here detailed measurements of mean flow fields were carried out by laser-Doppler anemometry at inlet duct Reynolds numbers of Kozicki (1966) (Re*) of 200 pertaining to the laminar flow regime. The two non-Newtonian fluids were aqueous solutions of xanthan gum (XG) and polyacrylamide (PAA) at weight concentrations of 0.2% and 0.125%, respectively. For Newtonian fluids, Cavadas et al (2006) found a characteristic three-dimensional helical flow inside the recirculation, starting at the symmetry plane and evolving towards the flat side walls. This helical flow eliminates the separated flow region near the side walls and was also visualized in the non-Newtonian cases. Before reaching the flat side walls, the fluid in helical motion exits the recirculation and joins the main flow stream creating a near-wall jet which can be seen as velocity peaks near the walls in the spanwise profiles of streamwise velocity. The numerical simulations investigated the roles of shear-thinning and inertia on the main flow characteristics for purely viscous fluids at Reynolds numbers between 10 and 800. The length of the recirculation (X_R) is constant in the central portion of the channel and decays to zero before reaching the flat side walls. At high Reynolds numbers a slight increase in X_R at the edge of the core of the flow is apparent. As expected, inertia increases the length of the recirculation as for Newtonian fluids, but somewhat surprisingly it also increases the three-dimensional nature of the flow by reducing the size of the central core. Shear-thinning enhances the role of inertia especially at high Reynolds numbers, whereas at low Reynolds numbers the behavior is quite similar for all fluids. All flow fields were found to be symmetric relative to x-z and x-y centre planes.

1. Introduction

High velocity impinging jets are frequently used in industry to cool metals and process food and pharmaceutical products, Sarkar et al (2004), because of the large increase in heat and mass transfer they promote near the impact surface. The objective of this work is the investigation of flow patterns of isothermal laminar impinging rectangular jet flows, confined by inclined and plane walls, for some non-Newtonian liquids.

Liquid single-phase impinging jets are usually either submerged or free-surface jets. In submerged jets the liquid issues into a region containing the same liquid at rest, whereas in free-surface jets the liquid jet is surrounded by ambient air or gas. Submerged jets can be unconfined or confined by a surface; in the latter case, there is usually a plate attached to the nozzle and parallel to the impinging surface, but such plate can also be inclined.

This work investigates laminar impinging jet flows, confined by sloped plane walls where the non-Newtonian fluids were aqueous solutions of xanthan gum (XG) and polyacrylamide (PAA) at weight concentrations of 0.2% and 0.125% respectively. These inclined confining walls extend

from the exit of a rectangular duct to a short distance above the impinging plate.

The experiments help to understand the flow dynamics and the differences in relation to the corresponding Newtonian laminar flow. They also validate results of some numerical calculations included to explore the effects of rheological parameters into the flow dynamics. The next section describes the experimental setup and the instrumentation used, including the laser Doppler anemometer. Experimental results are presented and discussed in section 3, followed by a brief description of the numerical method and the corresponding results in section 4

2. Experimental set-up

2.1 Experimental facilities

The flow loop used in the present experiments is shown schematically in. Flow was provided by a progressive cavity pump [2] (mono pumps Dresser model CB081AC1A3/G, the numbers in brackets refer to components shown in) fed directly from a stainless steel tank of 175 l of capacity [1]. One pulsation damper [3], located immediately downstream of the mono pump outlet, was used to smooth out the flow and remove any pulsations prior to the inlet to the entrance reservoir [5]. At the top of this reservoir, an air chamber dampened any residual pulsations in order to have a complete steady flow at the rectangular duct inlet. The rectangular duct [6] was made of four modules and was 2.6 m long with an internal cross section area of 0.0052 m^2 (height (H) x width (2*W) = 0.02 m x 0.26 m, corresponding to an aspect ratio (AR) of 13). Each module was constructed from stainless steel plates, machined and ground to size and then assembled with screws and a bonding agent.

The cell test section [7] is schematically represented in Fig. 2 (a), together with the coordinate system used in this work (*x* and *y* are in the paper plane and *z* is in the normal direction; the origin is at the central point of the rectangular duct exit plane). A photo in Fig. 2(b) shows the test section. Two slopping plane walls, each making an angle of 12° relative to the flat surface (plate), confined the jet flow inside the cell. The outgoing flow was from two rectangular channels with 4 mm height (h) and the same width as the inlet rectangular duct, thus defining here AR=65. The reservoirs [5] and [7] and the test cell were made of acrylic to allow velocity measurements using a laser Doppler anemometer (LDA).

Eleven pressure taps were drilled along the rectangular duct *x*-*y* center plane with 200 mm spacing between consecutive taps. They were used to study the development of the flow along the duct. The pressure measurements helped ensure that the connections between the duct modules (manufactured with machining tolerances of $\pm 10\mu m$) did not produce any detectable perturbation to the flow . The pressure differences between any two taps were measured by a differential pressure transducer, model P305D-S20 from Valydine. The transducer calibration was carried out in a device made up of two independent water columns with the water level checked by two precision rules with an accuracy better than 0.1 mm. All pressure taps were drilled carefully to avoid spurious edge effects. For the design of pressure taps the recommendations of Shaw (1960) and Franklin and Wallace (1970) were followed.

An electromagnetic flowmeter, type Mag Master [4] from ABB Taylor, measured the volumetric flow rates ($\dot{Q}_{in}$) in the range of 0-5 l/s with an accuracy of 0.2% of full scale.

All the instruments were connected to a 486 PC provided with a data acquisition board interfaced with an Advantech PCLD-8115 card.

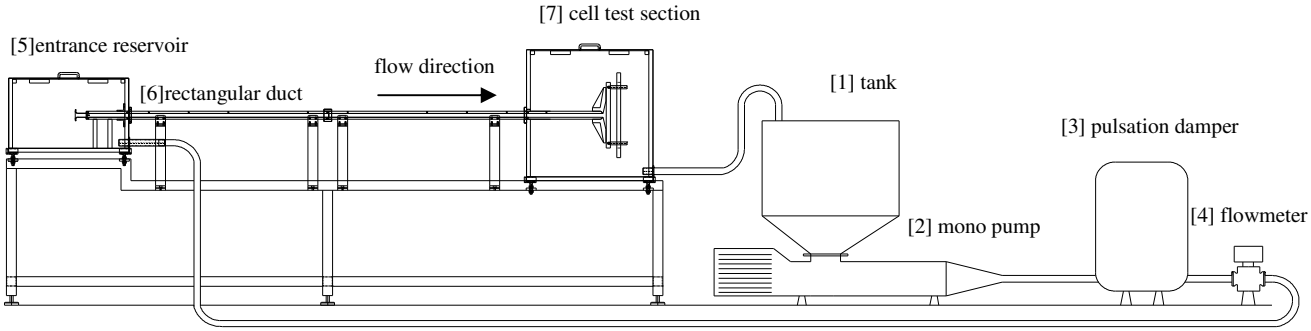

Fig. 1 Schematic of flow loop.

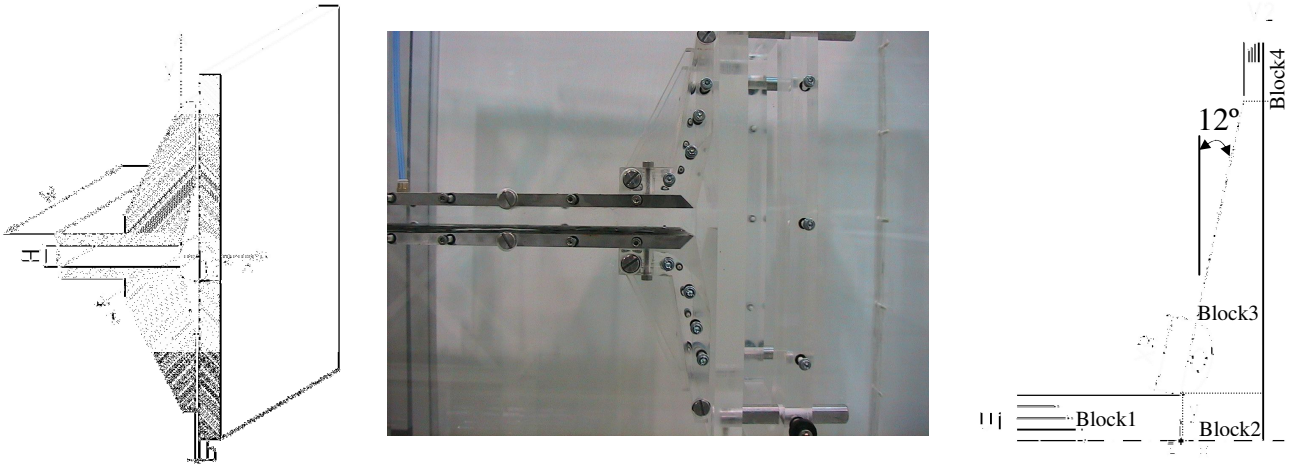

(a) (b)

Fig. 2 – Cell test section: (a) sketch of the half cell test section and coordinate system centered in the *x-y* and *x-z* plane; (b) photo of the cell test section (c) measured values and blocks used in the numerical simulation.

2.2 Laser-Doppler system

A 1-D laser-Doppler anemometer from Dantec was used to measure the mean and fluctuating velocity fields. The LDA was used in the forward scatter mode and the light source was an air-cooled, multimode 300 mW Ar-ion laser. The beam passed through a series of optical elements before the Bragg cell, where a frequency shift of 0.6 MHz was imposed. The front lens had a 300 mm focal length. The scattered light was collected by a photo-multiplier before which stood an interference filter of 514.5 nm. After being band-pass filtered, the signal from the photo-multiplier was processed by a TSI 1990C counter operating in the single measurement per burst mode with a frequency validation setting of 1% in the 10/16 cycle comparison. A 1400 Dostek card interfaced the counter with an 80486 based computer to provide all the statistical quantities via a purpose-built software. For each point measured, a sample size of 10000 values was taken. The refraction of the laser beams at the plane walls of the duct and of the cell was taken into account to correct the position of the control volume. Table 1 provides the main characteristics of the LDA.

The LDA probe was mounted on a milling table with movement in the three spatial coordinates. The system was used to measure both the mean and fluctuating velocities in the horizontal (u and u`) and vertical ($v$ and $v$`) directions along the duct and inside the cell. For the horizontal velocity component inside the rectangular duct the laser beams were set to cross each other in a horizontal plane and measurements could be performed in the viscous sublayer.

Laser wavelength	514.5 nm
Measured half angle of beams in air	3.65°
Dimensions of the measuring volume in air	
major axis	2.53 mm
minor axis	146 μm
Fringe spacing	4.041 μm
Frequency shift	0.6 MHz

Table 1 - Main characteristics of the LDA in air at e^{-2} intensity.

Near the sloped wall, inside the cell, the horizontal velocity component could not be measured directly because one of the beams collided with the wall. In such cases, the *u* velocity component was determined using trigonometry and measurements of the vertical velocity component and of a velocity component at an angle of 24º with the vertical direction. Because of optical access, these velocity measurements inside the cell were not performed at the centre-plane, but at a plane (z/W = 0.45) closer to the side wall, where the end wall did not affect the flow, as will be shown in Section 4. Typical uncertainties associated to the mean and fluctuating streamwise velocity data were estimated to be 1 % and 4 %, respectively. These uncertainties increased to 2% and 5% for transverse mean and fluctuating velocities and to 3.5% and 14% for the indirectly measured mean and fluctuating horizontal velocities inside the cell, respectively.

2.3 Fluid rheology

Measurements of the flow field were carried out with two aqueous polymer solutions based on two different polymers. The non-Newtonian fluids used were xanthan gum(XG) and polyacrylamide (PAA). The XG is a food-grade polymer with a high molecular weight (supplied by the Kelco Division of Merck) and was added at a weight concentration of 0.2%.The PAA is a polymer with a high molecular weight (reference Separan AN-934 SH) and was added at a weight concentration of 0.125%. To prevent bacteriological degradation, 0.02% by weight of biocide kathon LXE from Rhom and Hass was added to all fluids.

All solutions were prepared with Porto tap water following the same procedure. The additives were added slowly to the water while being stirred, after which the mixtures were agitated for further 90 minutes. The solutions rested for 24 hours to ensure complete hydratation of the molecules, and prior to any rheological or hydrodynamic measurement the solutions were agitated again for 30 minutes to fully homogenization. During the experiments, the temperature was monitored in order to accurately determine the correct fluid properties.

The rheology of the fluids was measured in a rheometer (TA-AR 2000) implemented with a cone-plate geometry. The variation of the viscometric viscosity with shear rate of the two solutions is plotted in Fig. 3 (a). Viscosity models were fitted to the measured data by a least square method. For both solutions, we fitted the power law model (equation (1)) and the Carreau-Yasuda model equation ((2)). In these models, K represents the indice of consistence and n the indice of behavior. The parameters of the adjusted viscosity models are tabulated in table 2.

$$\eta(\dot{\gamma}) = \mathrm{K}(\dot{\gamma})^{\mathrm{n}-1} \tag{1}$$

$$\eta(\dot{\gamma}) = \eta_\infty + (\eta_0 - \eta_\infty)\left[1 + (\lambda\dot{\gamma})^a\right]^{\frac{n-1}{a}} \qquad (2)$$

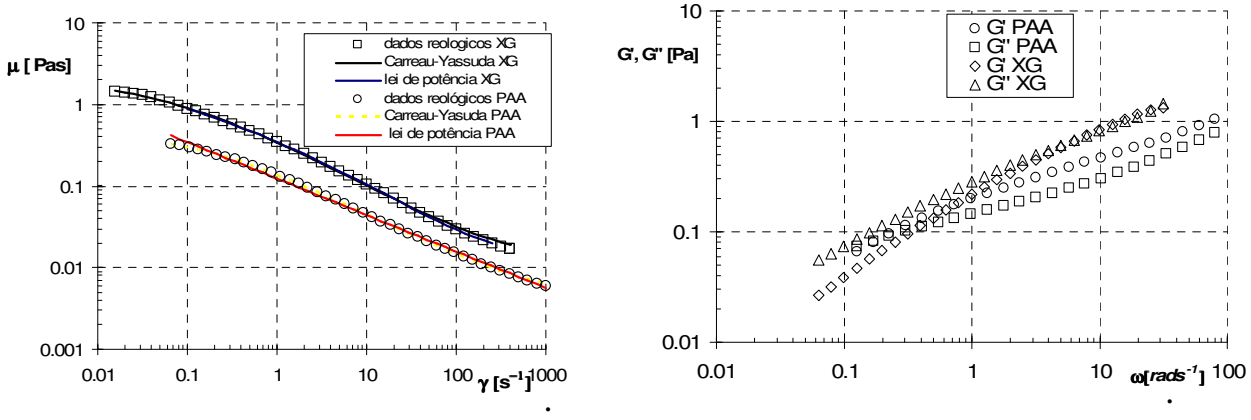

(a) (b)

Fig. 3 – Rheology of the two polymer solutions at 25ºC (a) Measured viscometric viscosity (b) Dissipation (*G''*) and conservation (*G'*) module

Fluido	ρ [kg/m^3]	μ_0 [Pa.s	μ_∞ [Pa.s]	λ [s]	a	n	K [Pa.s^n]
Glycerol-Water	1184	--------	--------	-------	-------	1	0.0425
0.2% XG	1000	2.3242	0.00996	11.6875	0.50339	0.3454	-------
0.2% XG	1000	-------	-------	------	------	0.491	0.324
0.125% PAA	1000	0.4378	0.00314	5.6179	0.7422	0.4285	-------
0.125% PAA	1000	-------	--------	-------	-------	0.5534	0.1234

Table 2 Parameters of Carreau-Yasuda and power law models adjusted to the Newtonian and non-Newtonian solutions.

In Fig. 3 (b) the dissipation (*G´´*) and conservation (*G´*) module are presented for the two solutions. For both fluids *G´´* is slightly higher than *G´* indicating that the solutions are moderately elastic.

3. Experimental results

3.1 Fully-developed flow in the rectangular duct

For flow in non-circular ducts and also when non-Newtonian fluids are involved the matter of Reynolds number definition is an important one. The Reynolds number used here, Re* in equation (3), was defined by Kozicki et al.(1966). The generalized Kozicki Reynolds number is based on the mean inlet velocity, *U*, measured by the flowmeter, and the length scale is the hydraulic diameter of the rectangular channel. Parameters *a* and *b* take on the values of a = 0.4311 and b=0.9281 for an aspect ratio of 13. The velocity data are normalized with the bulk velocity at the rectangular channel, the *x* and *y* coordinates are made non-dimensional by the height of the inlet duct (*H*) and the *z* coordinate by the half-width of the channel (*W*). All the experimental data reported in this section pertain to Re*=200, unless otherwise stated.

$$\mathrm{Re}^* = \frac{\rho(U)^{2-n} D_H^n}{8^{n-1} k\left(b + \frac{a}{n}\right)^n} \qquad (3)$$

Transverse profiles of streamwise velocity were measured along the rectangular duct and compared with theoretical expressions for fully-developed flow. They are shown in Fig. 4 (a) and Fig. 5(a) for the XG and PAA solutions, respectively and were measured at *x/H*= -5.7. The figures also include theoretical data for the parallel plate flow (AR=∞) as well as data for a Newtonian fluid at the same Kozicki Reynolds number. The data for the PAA solution lies on the theoretical curves whereas for the XG solution there is a difference of 2% well within experimental uncertainty. The symmetry relative to the *x*-*y* centre-plane was measured and the corresponding spanwise profiles of streamwise velocity at *x/H*= -0.4 are shown in Fig. 4 (b) and in Fig. 5 (b), for the XG and PAA solutions, respectively. The filled symbols represent the reflected profile from one half of the duct into the other half. The flow is symmetric and the presence of the end walls is not felt in the bulk of the flow, between *z*/W = ± 0.6 for XG solution and *z*/W = ± 0.5 for PAA solution.

We can see that the velocities in the center of the duct for the non-Newtonian solutions are lower than from the Newtonian solutions because of the shear-thinning behaviour of the non-Newtonian solutions.

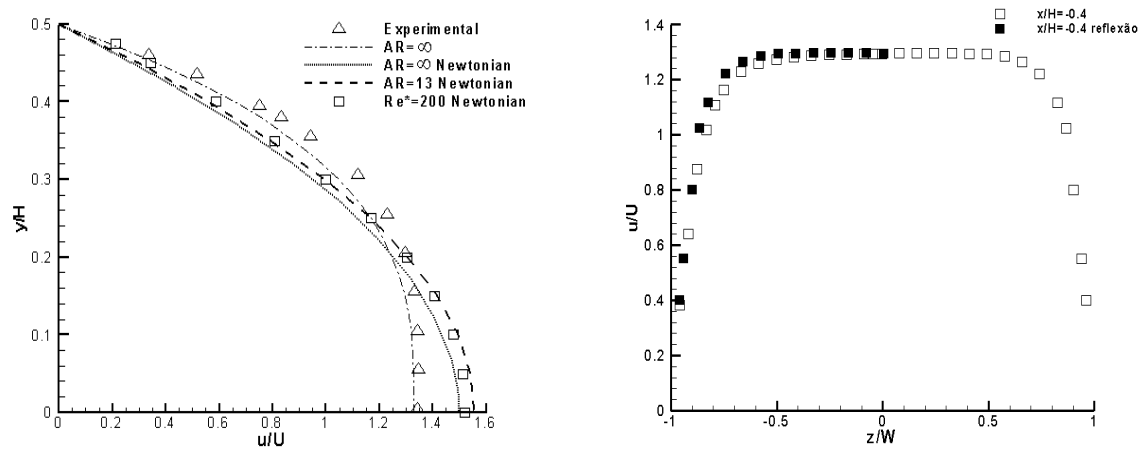

(a) (b)

Fig. 4 – Comparison between measurements (symbols) and theoretical data (lines) for solution 0.2% XG at Re*=200; (a) streamwise velocity profile at *x/H*= -5.7; (b) Spanwise profiles of streamwise velocity at *y/H* =0, *x/H*= -0.4.

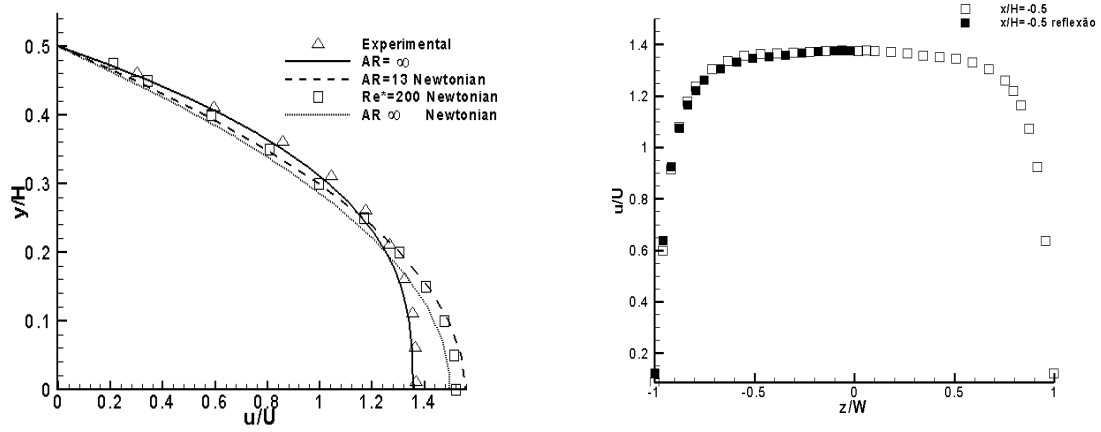

(a) (b)

Fig. 5 – Comparison between measurements data (symbols) and theoretical data (lines) for solution of 0.125% PAA at *Re**= 200: (a) Streamwise velocity profile at *x/H*= -5.7; (b) Spanwise profiles of streamwise velocity at *y/H* =0, *x/H*= -0.4.

3.2 Flow pattern within the cell

The progression of the streamwise velocity at the end of the rectangular duct and in the impinging jet region is shown in Fig. 6 (a) (b) and (c) along the *x*-*y* centre-plane for the XG and PAA solutions, respectively, including data for the Newtonian fluid case at the same Reynolds number, which is represented with closed symbols. The first profile, at *x*/*H*=-5.7, corresponds to the fully-developed flow. For the Newtonian fluid data at *x*/*H*=-0.4 the effect of the plate is still rather weak, with values of velocity differing from the fully-developed profile by less than 2.5 %. For the non-Newtonian solutions, this difference is higher especially for the PAA solution. The decrease of velocity near the centreline and the flow acceleration near the walls are clearly seen as the fluid approaches the plate, especially after the fluid exits the rectangular duct, i.e., when there is a large drop in *u*-velocity and the no-slip condition ceases to apply because the upper and lower walls are absent. Fig. 6 (a) and (b) also show symmetry relative to *x*-*z* centre-plane. As happen in the entrance duct we can see that the velocities, for the same position, in the central plane are higher for the Newtonian case. This fact is related to the shear-thinning behaviour of the solutions used.

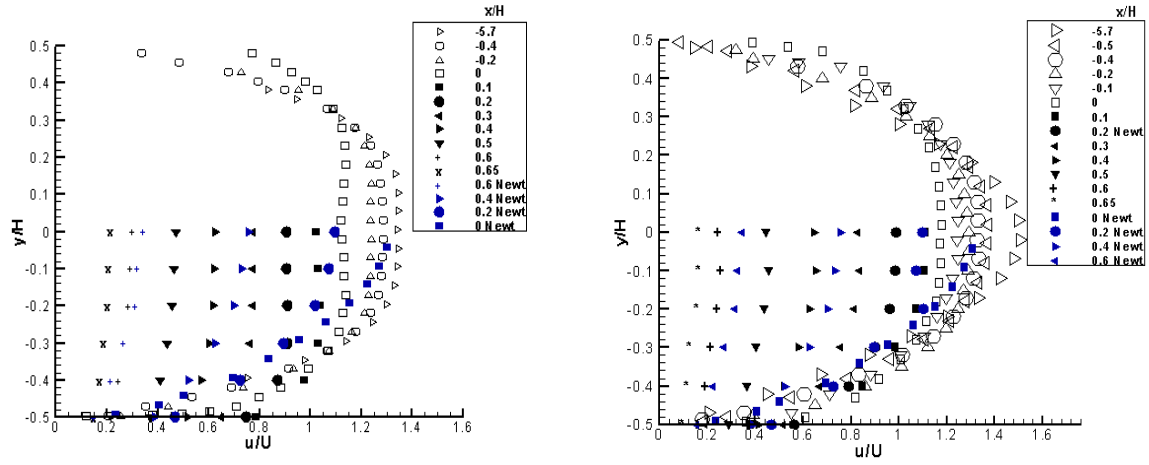

(a) (b)

Fig. 6 – Flow at the end of the duct and in the impact region for Re*=200, transverse profiles of streamwise velocity; (a) for 0.2% XG solution and Newtonian solution; (b) for 0.125% PAA solution and Newtonian solution .

With all fluids, a recirculation zone near the slopping plane walls was observed, as can be seen in Fig. 7 were profiles of the vertical velocity component inside the cell are plotted. Fig. 7 (a) plots Newtonian data for Re*=100 and Re*=200; for Re*=100 there is no recirculation zone and for Re*=200 the length of the recirculation is X_R/H =0.25. Fig. 7 (b) and (c) plot the corresponding profiles at Re*=200 for the XG and PAA solution, respectively. The length of the recirculation are X_R/H =0.35 and X_R/H =0.30, respectively, showing that the non-Newtonian behavior enhances the recirculation zone.

The flow symmetry inside the cell relative to *x*-*z* centre-plane for the XG and PAA solutions are shown in Fig. 8 (a) and (b), respectively. Transverse profiles of the streamwise velocity inside the 4 mm (*h*) wide channel and the profiles at two symmetric stations (*x*/*H*= ±4.9) are compared (the velocities at *x*/*H*= -4.9 are negative and hence were multiplied by (-1). In both non-Newtonian solutions the differences between the two velocity profiles is very small showing that there is symmetry relative to *x*-*z* centre-plane. Note that these profiles are here normalised by the inlet duct bulk velocity rather than by the local bulk velocity.

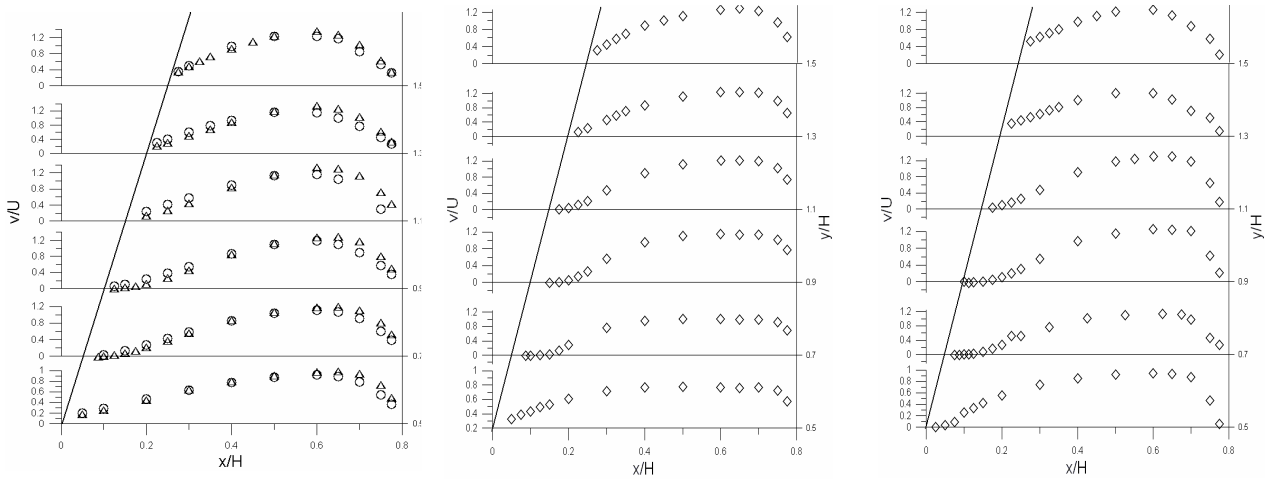

(a) (b) (c)

Fig. 7 – Vertical velocity profiles at *z*/W=0.45 in the cell (a) Newtonian, O Re*=100 and Δ Re*=200; (b) 0.2%Xg at Re*=200; (c) 0.125% PAA at Re*=200.

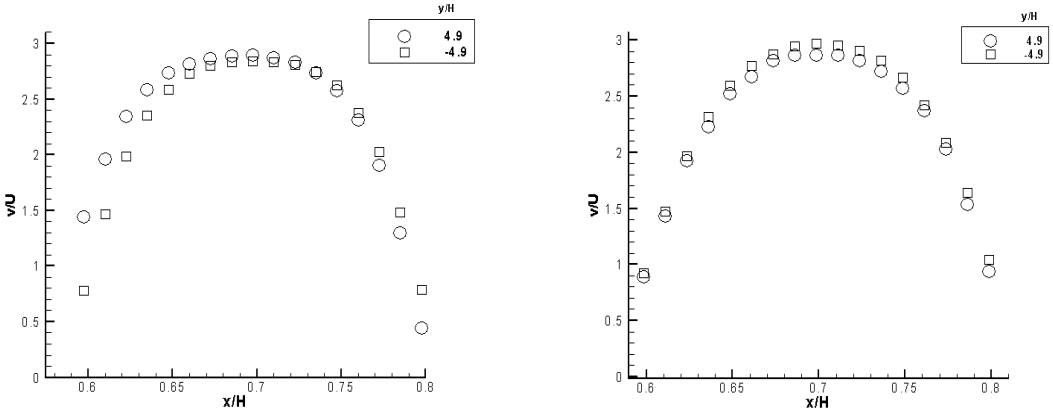

(a) (b)

Fig. 8 – Transvers profiles at *y*/*H*=4.9 *y*/*H*=-4.9 in the plane *z*/*W*=0.45 at Re*=200 (a) 0.2% XG (b) 0.125% PAA.

3.3 Three dimensional effect

Some spanwise profiles of the vertical velocity measured inside the cell are plotted in Fig. 9 (b) and (c) for the solution of XG and PAA, respectively, including Newtonian fluid data at the same Re*=200. These show that local maxima and minima in the vertical velocity are stronger near the slopping wall and at the beginning of the narrowing cell. Simultaneously, no separated flow regions zones were seen near the flat side walls. Visualizations of the flow using a die injection technique, but especially small tracer bubbles, and a video camera, have shown a helical flow motion depicted schematically in Fig. 9 (a).

Before reaching the end walls, the fluid in helical motion exits the separated flow region, which vanishes, and merges with the main flow creating a vertical wall jet. The wall jets are the peaks of vertical velocities seen near the end walls (at *z/W*≈ -0.9 for *y/H*= -1.65, *x/H*=0.525), just downstream the separated flow. Further downstream along the converging channel the jet weakens and the velocities rise due to continuity. Still, there are traces of a perturbation in the velocity profiles (*z/W*≈ -0.95 for *y/H*= -3.1, *x/H*=0.675). For the PAA solution, the peak is stronger than the peak for the XG solution and they are both stronger than for the Newtonian fluid as we can see in

Fig. 9 (b) and (c), showing that the non-Newtonian behavior enhances the strength of the helical flow and consequently the near wall jet. The closed symbols are the reflection of the velocity profile on one side of the duct onto the other half showing that there is symmetry relative to *x-y* centre-plane.

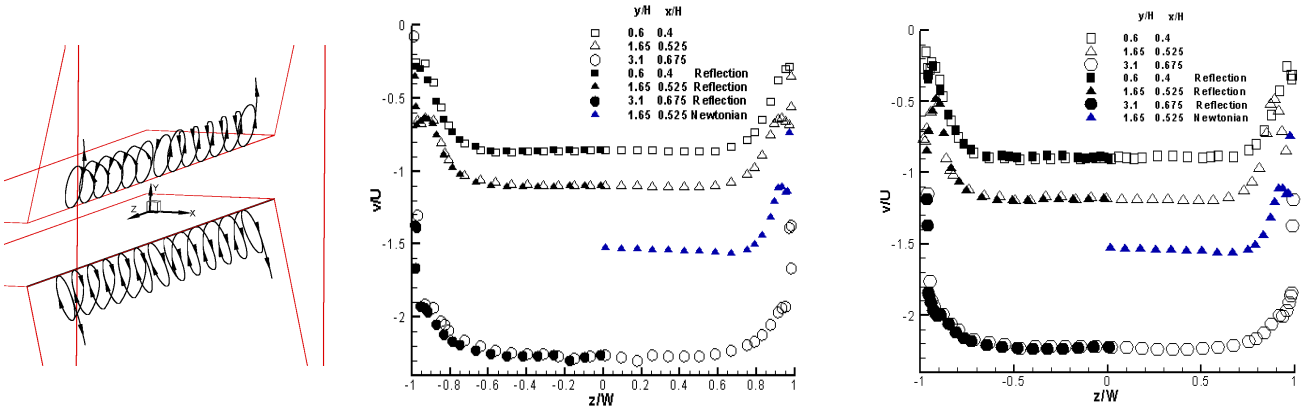

(a) (b) (c)

Fig. 9 – (a) Sketch of the three-dimensional flow in the separated flow region; Spanwise profiles of streamise velocity at various locations for Re*=200 (b) 0.2% XG (c) 0.125% PAA.

4. Numerical predictions

Numerical predictions of these flows were carried out and they were validated against the Newtonian measurements of Cavadas et al. (2006). A in-house finite volume code was used, which has been extensively used and validated in several other occasions (Oliveira et al. (1998), Pinho et al. (2003)). For conciseness, the description of the method is very brief since it is also described in those works. The code solve the three-dimensional time dependent governing equations for Newtonian and various inelastic and viscoelastic non-Newtonian fluids, including the power law fluids. The code uses non-Orthogonal collocated grids and the discretization and interpolation schemes were at least second order. In particular central differences were used for the diffusion terms and the high-resolution method CUBISTA, Alves (2003), was used for the convective terms. The solution algorithm was a modified version of the SIMPLEC algorithm of van Doormal and Raithby (1984) adapted for time marching as explained in Issa and Oliveira (1994), where details to evaluate mass fluxes at cell faces can be found.

The computational grids were generated using patched blocks, one for the inlet of the channel, two for the cell zone, and one for the outlet of the channel. A schematic representation of the blocks used in the numerical simulations is shown in Fig. 2 (c). The mesh was non-uniform, with more control volumes (CV) in the cell zone for accurate predictions. The expansion factors used were carefully chosen to guarantee a smooth variation of the CV across the whole domain, in particular at the interfaces between the mesh-generating blocks. After tests on the adequacy of the computational domain and mesh size to ensure grid-independent results, the finest grid selected had a total number of 835200 CVs with 30 CVs spanning the half-height of the channel. Flow symmetry relative to planes x-y and plane x-z was considered (Fig. 2 (c)) based on experimental work and preliminary numerical tests, so only a quarter of the domain was mapped. On the centreline, an axisymmetric condition was assumed, and at the wall, all the velocity components were set to zero. At the inlet of the duct, the flow profile was set as uniform very much as at the rig. Neumann conditions were set at the outlet for velocities and the pressure gradient.

The fluids used in the simulations are described by a power law model (equation (1)) and the

predictions compared well with experimental results for Newtonian fluids. Since the constitutive equation adopted was purely viscous and the fluids are viscoelastic, the comparisons were not as good as for Newtonian fluid. Nevertheless, this set of computations with the power law fluids help determine the effects of shear-thinning on flow dynamics. Viscoelastic simulations are currently being carried out, but they are still incomplete and are not reported here.

Fig. 10 (a) (b) e (c) compares predicted and measured velocity profiles for the 0.2% XG solution. The prediction are for the Carreau model of table 2 and the profiles are at positions x/H= -5.7 and z/W=0, y/H= 0.8 and z/W=0.45, x/H=0.525 and y/H= 1.65. There is good agreement between the two sets of data with a maximum difference of 10%, even though the xanthan gum solution is viscoelastic. This good agreement was the starting point to perform an extensive set of numerical calculations to investigate shear-thinning effects of the flow dynamics using a power law model.

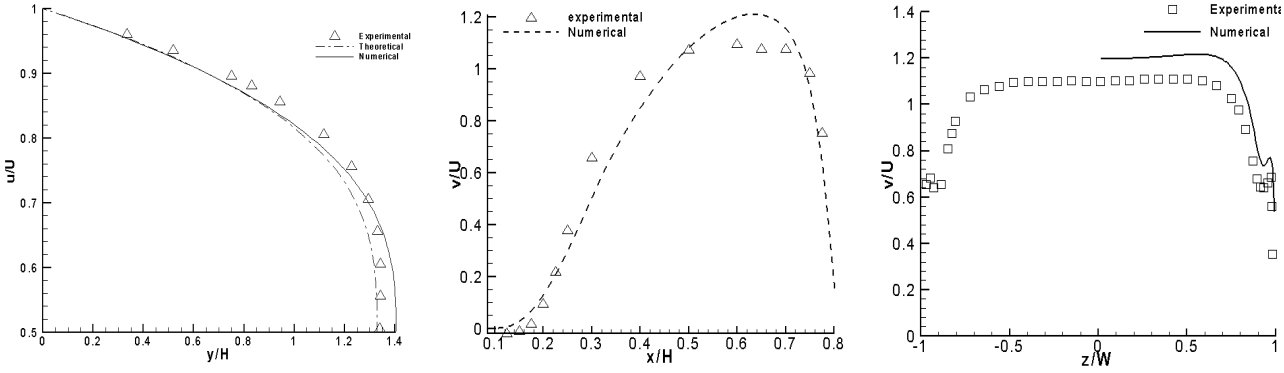

(a) (b) (c)

Fig. 10– Comparison between experimental data (symbols), theoretical expressions and numerical simulation results for the rectangular duct, xanthan gum at Re*=200; (a) at x/H=-5.7 z/W=0 (b) at y/H=0.8, z/W=0.45 (b) at y/H=1.65, x/H=0.525

Next, we show the variation of the recirculation bubble length (X_R) and we characterize numerically the evolution of this length along the third dimension (z).

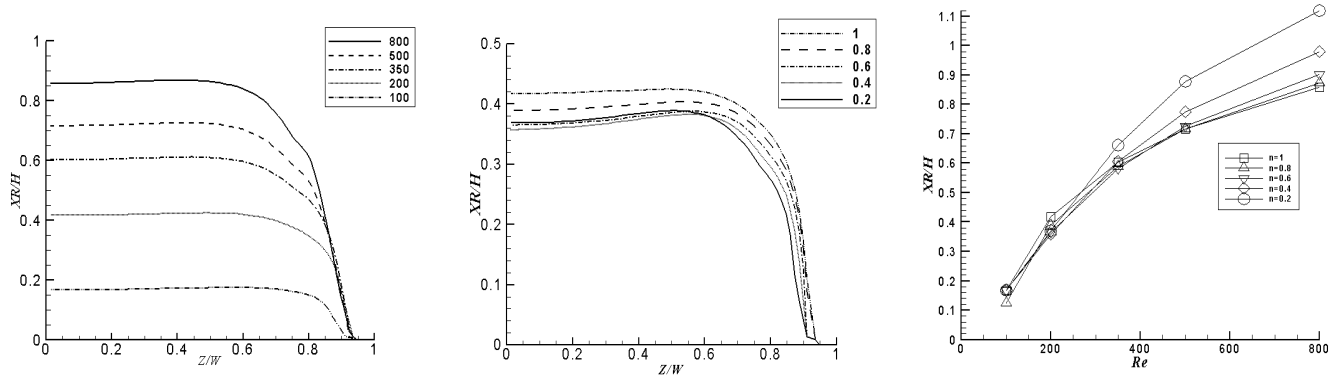

(a) (b) (c)

Fig. 11 Recirculation Length (X_R) along the

Fig. 11 (b) shows the influence of the power law index n for a constant Reynolds number (Re^*=200). There is a small increase in X_R as the power law index n increases. Along the spanwise direction (z/W) the recirculation length is almost constant for all values of n, with a slight increase near the sidewall especially for low values of the power index.

The combined influence of Re^* and n on X_R is plotted in Fig. 11 (c). It is clear that the largest effect of Reynolds number is for n=0.2 due to the strong shear-thinning nature of fluid, whereas at lower Reynolds numbers the influence of n is somewhat limited.

5. Conclusions

The flow field created by liquid impinging jets in a cell confined by a slopping plane wall was studied for Newtonian and non-Newtonian fluids using pressure transducers and laser-Doppler anemometry. The flow field in the approach rectangular duct was fully-developed prior to the cell and the flow in the center of the duct was not significantly influenced by the presence of the end walls due to the large aspect ratio used (AR=13). The flow was everywhere symmetric relative to the x-y and x-z centre-planes for Newtonian and non-Newtonian fluids.

The study indicates the presence of a small recirculation attached to the slopping wall, the size of which increased with Reynolds number. Their normalised lengths, X_R/H, are of 0.35 and 0.3 for the XG and PAA solutions, respectively and 0.25 for a Newtonian fluid at the same Reynolds number (Re*=200).

A three dimensional effect was found, which was characterized by a wall jet near the sidewalls, and concomitant the absence of a separated flow region. A symmetric helical motion of separated fluid was visualized from the x-y centre-plane towards the sidewalls, confirming the characteristics measured by LDA, for the Newtonian and non-Newtonian fluids. The wall jet is stronger for the PAA solution than for the XG solution and they are both stronger than for the Newtonian fluid, showing that the non-Newtonian behaviour enhances the strength of the helical flow and the near wall jet.

The numerical predictions for the Newtonian fluid compared very well with experimental data. For non-Newtonian fluids the predictions using a generalized model were not as good but nevertheless the differences were small, not exceeding 8%. The numerical predictions captured the 3D effects observed by flow visualization and provided physical insight. The calculations were carried out for Re* between 100 and 800 and showed that X_R increased with Re*, regardless the power law index, but shear-thinning made the behavior non-monotonic: at low Re* the largest value of X_R pertained to Newtonian fluids, whereas at large Re* the Newtonian fluids had the smallest value of X_R.

6. Acknowledgements

The authors acknowledge funding by FCT and FEDER via the budget of Centro de Estudos de Fenómenos de Transporte and projects POCI56342/EQU/2004 and PTDC/EQU-FTT/70727/2004 and A. S. Cavadas is grateful to FCT for the PhD grant BD/7091/2001.

7. References

Alves, M.A., Oliveira, P.J. and Pinho, F.T., "A convergent and universally bounded interpolation scheme for the treatment of advection", *Int.J. Numer. Meth. Fluids*, 47, 665-679, (2003).

Cavadas, A.S., Campos, J.B.L.M., Pinho, F.T. "Flow field in impinging jets confined by slopping plane walls". Proceedings of 13th International Symposium on Applications of Laser Techniques to Fluid Mechanics, paper 15.5 pdf, Lisbon, 26-29 June 2006, Portugal.

Dean, R.B.,"Reynolds number dependence of skin friction and other bulk flow variables in two-dimensional rectangular duct flow", *J. Fluids Eng.*, 100, 215 (1978).

Franklin, R.E., Wallace, J.M., "Absolute measurements of static-hole error using flush transducers", *J. Fluid Mech*., 42, 33-48, (1970)

Gardon, R. and J. C. Akfirat, "The role of turbulence in determining the heat transfer characteristics of impinging jets", *International Journal of Heat and Mass Transfer*, 8, 1261- 1272 (1965).

Garimella, S. V., and R. A. Rice, "Confined and submerged liquid jet impingement Heat transfer", *ASME J. Heat Transfer*, 117, 871 (1995).

Issa, R.I., Oliveira, P.J., "Numerical predictions of phase separation in two-phase flow through T-junctions", *Comput. Fluids*, 23, 347-372 (1994)

Kim, J., Moin, P., Moser, R., "Turbulence statistics in fully developed channel flow at low Reynolds numbers", *J. Fluid Mech.* 177, 133-166 (1987).

Kozicki, W., Chou, C. H. and Tiu, C., "Non-Newtonian flow in ducts of arbitrary cross-sectional shape", *Chemical Engineering Science,* 21, 665-679 (1966).

Martin, H., "Heat and Mass transfer between impinging gas jets and solid surfaces", *Adv Heat Transfer*, 13, 1 (1977)

Oliveira, P.J., "Compute modeling of multidimensional multiphase flow and application to T-junctions", Ph.D. thesis, Imperial College, London, U.K., (1992)

Oliveira, P.J., Pinho, F.T., Pinto, G.A. "Numerical simulation of non-linear elastic flows with a general collocated finite-volume method", *J. of Non-Newtonian Fluid Mechanics*, 79, 1-43 (1998)

Pinho, F.T., Oliveira, P.J. and Miranda, J.P. "Pressure losses in the laminar flow of shear-thinning power law fluids across a sudden pipe expansion", *Int. J. Heat & Fluid Flow*, 24, 747-761 (2003)

Shaw, R., "The influence of hole dimensions on static pressure measurements", *J. Fluid Mech*., 7, 550-564 ((1960)

Sarkar, A., Nitin, N., Karwe, M.V., Singh, R. P., "Fluid flow and heat transfer in air jet impingement in food processing", *Journal of Food Science*, 69, 113-122 (2004)

Van Doormal, J.P., Raithby, G.D., "Enhancements of the SIMPLE method for predicting incompressible fluid flows", *Numerical heat transfer*, 7, 147-163 (1984)

White, F. M., "Viscous Fluid Flow",2nd ed. *McGraw-Hill*, (1991).